


RESEARCH ARTICLE

Open Access



Magnetic-free chiral eigenmode spectroscopy for simultaneous sensitive measurement of optical rotary dispersion and circular dichroism

Wenpeng Zhou^{1,2†}, Ya-Ping Ruan^{1,2†}, Haodong Wu^{1,2†}, Han Zhang^{2,3†}, Jiang-Shan Tang^{1,2}, Zhenda Xie⁴, Lei Tang^{1,2}, Yu Wang^{1,2}, Yue-E Ji^{1,2}, Kunpeng Jia⁴, Cheng-Wei Qiu^{5*}, Yan-Qing Lu^{1,2*} and Keyu Xia^{1,2,6*} 

Abstract

Chirality, defined by Lord Kelvin, refers to the geometric symmetry property of an object that cannot be superposed onto its mirror image using rotations and translations. The material's chirality can be probed with light as the optical activity: optical rotary dispersion (ORD) and circular dichroism (CD). It is still challenging to yield extremely sensitive ORD and CD for very weak chirality and measure both simultaneously. Cavity ringdown polarimetry has been reported to improve ORD detection sensitivity with the absence of equally important CD signature, at the price of high cavity finesse near 400, frequency-locking sophistication, and large magnetic field. Here, we report a unique recipe to demonstrate the simultaneous measurement of ORD and the CD by separately observing the chiral eigenmode spectra from a bowtie optical cavity with a finesse about 30, without resorting to frequency locking or magnetic field. We obtain a sensitivity of $\sim 2.7 \times 10^{-3} \text{ deg}/\sqrt{\text{Hz}}$ for ORD, $\sim 8.1 \times 10^{-6}/\sqrt{\text{Hz}}$ for CD, and a spectral resolution of 0.04 pm within a millisecond-scale measurement. We present a cost-effective yet ultrasensitive account for chiral chromatography, the conformational dynamics and chiroptical analysis of biological samples which particularly exhibit weak and narrow spectral signals.

Keywords Chiral material, Optical rotary dispersion, Circular dichroism, Cavity-enhanced chiral eigenmode spectroscopy

[†]Wenpeng Zhou, Ya-Ping Ruan, Haodong Wu and Han Zhang have contributed equally to this work.

⁶ Hefei National Laboratory, Hefei 230088, China

*Correspondence:

Cheng-Wei Qiu
chengwei.qiu@nus.edu.sg

Yan-Qing Lu
yqlu@nju.edu.cn

Keyu Xia
keyu.xia@nju.edu.cn

¹ College of Engineering and Applied Sciences, Nanjing University, Nanjing 210023, China

² National Laboratory of Solid State Microstructures, Nanjing University, Nanjing 210023, China

³ School of Physics, Nanjing University, Nanjing 210023, China

⁴ School of Electronic Science and Engineering, Nanjing University, Nanjing 210023, China

⁵ Department of Electrical and Computer Engineering, Engineering Drive 3, National University of Singapore, Singapore 117583, Singapore

1 Introduction

Chirality is a universal phenomenon throughout nature, ranging from inorganic to organic and from classical [1–4] to quantum materials [5–8]. It reveals the spatial chiral structure of matter [3, 4] and the three-dimensional arrangements of molecules within the macromolecular substance [9, 10]. Chiral molecules can be used to manipulate electronic spin orientation and related physical and chemical processes [11–13]. Most life-related macromolecules on Earth only exist in a single conformation, either right-handed or left-handed enantiomers [14, 15], displaying chirality. The study of the homochirality of biomolecules conformation may reveal the mystery of the origin of life [16, 17]. Chiral materials (CMs) exhibit optical activity such as the optical rotary dispersion (ORD) and the circular dichroism (CD). The artificial chiral nanostructures can even display a giant optical activity [3, 4, 18, 19]. The chiroptical analysis of material optical activity is significantly important, in particular, in the pharmaceutical industry, because changes in the drug's chirality can lead to ineffectiveness or even toxicity (e.g., thalidomide) [20].

Sensitive detection of the ORD and CD provides a powerful and preferable tools for chiroptical analysis. This method allows non-destructive characterization of biomolecular samples [10]. The ORD manifests the relative orientation of the electronic and magnetic dipole moments of a molecule by detecting the polarization rotation of a linearly polarized light through a medium [21]. The CD reflects the differential absorption of the right and left circularly polarized (RCP and LCP) light in a medium, determining the differential circularly polarized electronic dipole moment of a molecule. The strong atomic CD due to the asymmetric electronic dipole moments has been exploited to obtain quantum nonreciprocity [5, 22]. Both the ORD and CD are vital for determining the secondary structures of peptides and proteins [17, 23], the enantiomeric ratio of chiral drugs [24], and the three-dimensional structures of single chiral nanostructures [1, 25, 26].

For chiroptical analysis of molecules, simultaneously measurement of the ORD and CD with high spectral resolution and sensitivity is highly desired, because it is important for a great variety of biochemical applications, including time-resolved precise detection of the same “active” sample in the biological process, and characterization of molecular secondary structure. The conventional ORD polarimeters and CD spectrometers use light sources with power larger than 10 W, rely on different principles and configurations. Thus they can only measure the ORD and CD with difference devices, respectively. Moreover, they are limited to a low spectral resolution, up to about 10 pm, and long measurement

time, leading to a low temporal resolution and sensitivity. To improve the temporal resolution, the heterodyned detection method has demonstrated a measurement time of 60 fs by using a femtosecond laser [27], but at the expense of very low spectral resolution of 4 nm. To achieve a high sensitivity, various methods have been developed to enhance the chiroptical signals by using dual-comb spectroscopy [28], nonlinear resonant microwave spectroscopy [29], nonlinear absorption [15, 30], metasurfaces [24, 31], polarization-dispersion imaging spectroscopy [4], and cavity ringdown polarimetry [32–35]. Among these methods, the cavity ringdown polarimetry has a significant advantage in sensitivity because a high-quality cavity can greatly improve the effective interaction-path length with CMs. High-sensitivity ORD measurements are realized by using a four-mirror bow-tie cavity embedded with a magneto-optical Faraday medium and a strong permanent magnetic field [32–34]. Ultrasensitive CD measurement has been conducted via the cavity-based ringdown spectroscopy and polarimetry [35, 36]. Despite great success, to date, no single method has been widely adopted for simultaneously measuring both ORD and CD within the same cavity-based setup. For the purpose of simultaneous sensing of the ORD and CD signals, the sophisticated cavity-free interferometric Fourier-transform spectroscopy has been developed to analysis the optical activity of the free induction decay fields, which are emitted by the chiral material and amplified with the heterodyne detection [21, 37–39]. The ORD and CD can be retrieved from the chiroptical susceptibility, which is the chiral field normalized by the strong achiral one. In these methods, the achiral field, as a reference signal, needs to be measured separately. Moreover, they require precise mechanical control of the delay line and the orientation of polarizers.

This work reports the simultaneous measurement of absolute ORD and CD of CMs within a millisecond-scale measurement time by using the cavity-enhanced chiral eigenmode (CECEM) spectroscopy. Compared to the cavity ringdown polarimetry, our method is magnetic-free, only uses a single laser beam and operates without the need of precisely locking of the cavity frequency. Remarkably, unlike the interferometric Fourier-transform spectroscopy, it excludes any mechanical moving parts, significantly simplifying the implementation and operation. Experimentally, we achieve the ORD and CD sensitivities of $\sim 2.7 \times 10^{-3} \text{ deg}/\sqrt{\text{Hz}}$ and $\sim 8.1 \times 10^{-6}/\sqrt{\text{Hz}}$, respectively. These sensitivity are comparable to the previous methods (Fig. 1). In particular, we report a unprecedented spectral resolution of 0.04 pm. The CECEM spectroscopy with high resolution and sensitivity are essentially important for analysis of the molecular-vibration related optical

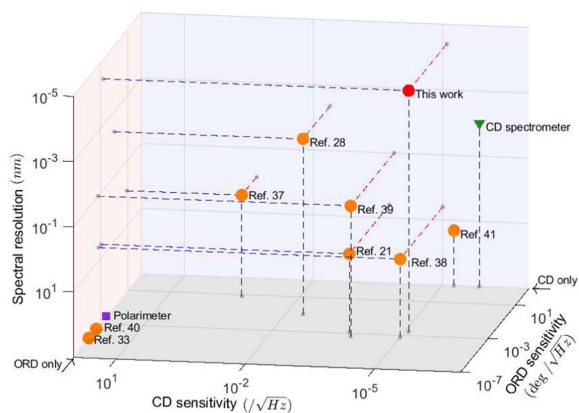


Fig. 1 Typical chiroptical measurement. Representative examples of optical activity measurement of varying designs and their measured performances. Orange circles correspond to the performances reported in various literatures, such as interferometric Fourier-transform balanced detection [21, 39] and active-heterodyne detection [37, 38] of the free-induction decay fields, dual-comb spectroscopy [28], cavity ringdown polarimetry [33, 40], and dispersive VCD instrument [41]. Purple squares to commercial ORD polarimeters (Anton Paar MCP500, Austria), and green triangles to commercial CD spectrometers (Applied Photophysics Chirascan V100, England). The experimental results of this work are represented by the red circle. In this comparison, the performances are characterized by the spectral resolution, the ORD sensitivity ($\delta_{\Delta\varphi} \times \sqrt{\tau}$) and the CD sensitivity ($\delta_{\Delta A} \times \sqrt{\tau}$), where $\delta_{\Delta\varphi}$ and $\delta_{\Delta A}$ are the standard deviations of the measured ORD and CD, respectively, and τ is the measurement time

activity, which typically has a very narrow characteristic spectrum [42–44].

2 Results

2.1 Concept

The key ideas of the cavity ringdown polarimetry and our CECEM spectroscopy method are compared with Figs. 2(a) and (b). Although both methods use a bowtie cavity comprising of four highly-reflective mirrors and embedded with a CM, our method can simultaneously measure the ORD and CD within a millisecond-scale measurement time, in comparison to the cavity ringdown polarimetry requiring a second-scale integration time. The experimental configuration is also essentially different from the cavity ringdown polarimetry in three points: (i) excluding the magnetic-optical effect; (ii) using a single input laser beam; (iii) measuring the transmission spectra of two eigenmodes. Thus, our system is simpler, more stable, and promises higher spectral resolution and shorter measurement time.

Notably, our CECEM spectroscopy cannot be conducted by inserting a CM in a standard two-mirror Fabry-Pérot (FP) cavity or a three-mirror ring cavity. Both types of cavities can support a pair of degenerate

LCP and RCP eigenmodes in the absence of the CM. The RCP light transforms into the LCP one after reflected by a mirror, and vice versa. Thus, in the standard FP cavity, the RCP and LCP eigenmodes accumulate the same phase shift and loss in the CM after a round trip in the cavity. Due to this compensation in opposite directions, the LCP and RCP eigenmodes are degenerate in resonance frequency and linewidth even in the presence of the CM. In the three-mirror ring cavity, the traveling eigenmodes need two round trips to recover their polarizations. As a result, the compensation issue remains. Because of the frequency and dissipation degeneracies, one cannot distinct the LCP and RCP eigenmodes in experiment by using the FP cavity or the three-mirror ring cavity.

Unlike the FP or three-mirror ring cavity, a four-mirror bowtie cavity shows an important advantage by tackling the compensation problem. It also supports the LCP and RCP traveling eigenmodes. These eigenmodes maintain their polarizations as they travel in the CM, simply because they suffers to four reflections and can recover their polarization after a single round trip. Therefore, after one round trip in the bowtie cavity, the LCP and RCP eigenmodes respectively accumulate different phase shifts and loss. Thus, the two eigenmodes are distinguishable in resonant frequency and linewidth. Therefore, the bowtie cavity can be used to measure the optical activity via the CECEM spectroscopy.

It has been a great success of utilizing the cavity ringdown signal to measure the ORD of a CM. The novel concept of a typical cavity ringdown polarimetry is schematically shown in Fig. 2(a). It measures the beating frequency of ringdown signals. First, two continuous-wave or pulsed linearly polarized laser fields can be input into the bowtie cavity with a precise angle θ to resonantly excite the counter-propagating clockwise and counter-clockwise modes. In comparison with a resonant pulsed laser can be applied [34, 45], however, a continuous-wave laser is preferable [32, 33]. This resonant driving requires precise frequency locking of the cavity mode. After that, the ringdown signals are created after a linear polarizer by suddenly switching off the input laser fields. The measurable beat in the output appears because the large external magnetic field B and the circular birefringence of the CM cause a detuning between the RCP and LCP eigenmodes. To effectively excite the cavity modes, the input laser field need to be very close to the resonance frequency of the high-Q cavity mode. Moreover, the lifetime of the cavity mode is much longer than the beat period to allow the appearance of the beating signal. As a result, the beating frequency limits the measurement time. The large magnetic field is used to induce a large zero-signal frequency splitting and thus provides a

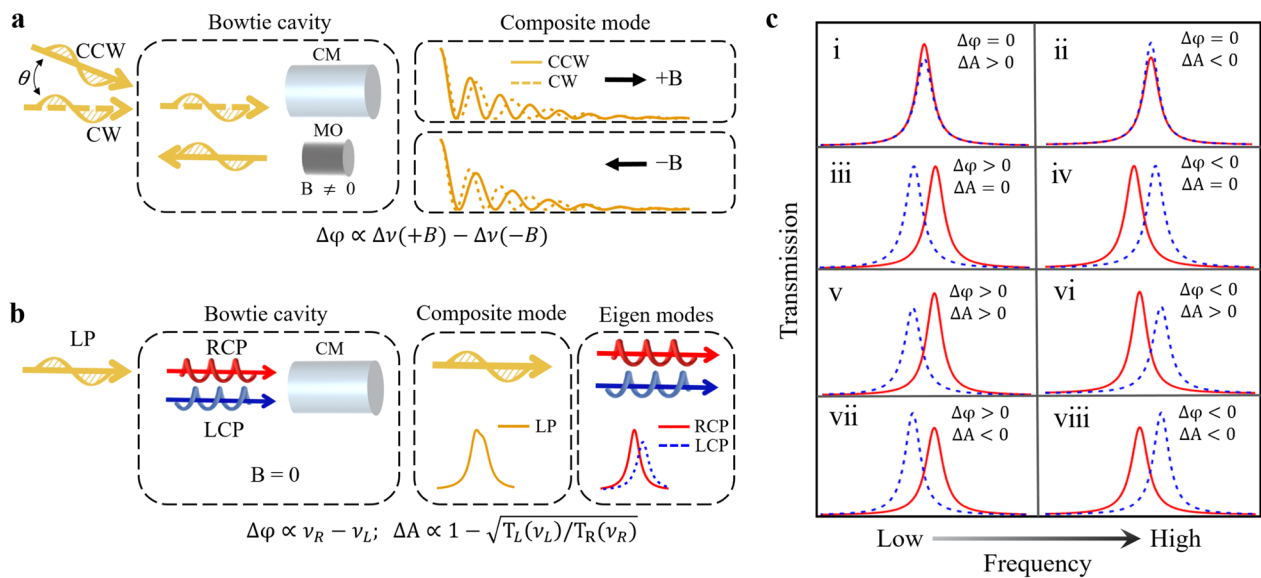


Fig. 2 Schematic of the ORD and CD measurement, respectively determined by $\Delta\varphi$ and ΔA . **a**, Cavity ringdown polarimetry. The chiral material (CM) and the magneto-optical (MO) Faraday material are inserted into a bowtie cavity. Two linearly polarized laser beams, arranged with a precise angle θ , resonantly drive the counter-propagating clockwise and counter-clockwise modes of the bowtie cavity. The composite outputs of these two modes exhibit as ringdown signals with a beating frequency $\Delta\nu(B)$. A magnetic field is used to provide a large initial beating frequency. By reversing the magnetic field B and measuring the beating frequency twice, the ORD of the CM is then determined by $\Delta\nu(+B) - \Delta\nu(-B)$. **b**, Magnetic-free CECEM spectroscopy method in this work. The bowtie cavity is only embedded with a CM but excludes the MO material. A single linearly polarized laser beam is used to simultaneously excite the LCP and RCP cavity eigenmodes. Instead of detecting the transmission of the composite field (yellow curves in the middle panel), the LCP (dashed blue curve) and RCP (solid red curve) eigenmode transmissions are measured separately. Thus, the ORD and CD can be precisely determined simultaneously from the difference of resonance frequency, $\Delta\varphi \propto \nu_R - \nu_L$, and the transmission peaks, $\Delta A \propto 1 - \sqrt{T_L(\nu_L)/T_R(\nu_R)}$. **c**, Schematic LCP (dashed blue curves) and RCP (solid red curves) transmissions for different ORD and CD

large bias for the beat frequency. The beating frequency $\Delta\nu(+B)$ can be retrieved from the ringdown signal by fitting, and limits the measurement time T_m such that $T_m \gg 1/\Delta\nu(B)$. By reversing the magnetic field, another beat frequency $\Delta\nu(-B)$ is measured. In the end, the ORD can be calculated from $\Delta\nu(+B) - \Delta\nu(-B)$. Moreover, due to frequency locking, the cavity ringdown polarimetry measures the ORD with high sensitivity at a single wavelength. The cavity ring-down methods are based on the interference between the polarization-filtered transmitted fields of two orthogonal eigenmodes. They can extract the ORD or CD of the CM, but are difficult to extract both simultaneously.

Our method of the CECEM spectroscopy is conceptually different, as depicted in Fig. 2(b). It can simultaneously measure the ORD and CD of the CM. Note that a linearly polarized field can be decomposed into the LCP and RCP components. We use a single linearly polarized laser beam to excite both the LCP and RCP cavity eigenmodes. Therefore, the LCP and RCP components share exactly the same optical path. Such a co-propagation arrangement makes our method robust against external perturbations caused by mechanical vibration and thermal drift, and also less demanding on precise alignment.

It can also avoid the fake signal resulted from the imperfect orientation of two input laser beam arrangement. Then, we scan the laser frequency and detect the output fields of the cavity. In the absence of the CM, these two modes are degenerate in resonance frequency and linewidth. The presence of the CM lifts the degeneracy of the resonance and linewidth. When the optical activity is very weak, it is difficult to distinguish the LCP and RCP eigenmode spectrum from the composite field (yellow linearly polarized spectrum). Instead of biasing the beat frequency of the LCP and RCP modes with a strong magnetic field as in the cavity ringdown polarimetry, we measure the transmission spectra of two LCP and RCP eigenmodes separately (red and blue spectra for the RCP and LCP modes). The ORD is proportional to the eigenmode frequency splitting, while the CD is determined by the differential transmission peaks of the spectra. Since the LCP and RCP eigenmode transmissions are separately detected by two detectors in two different optical paths, we can simultaneously detect extremely weak ORD and CD with high sensitivity. Remarkably, our method is magnetic free, and only needs a single frequency-tunable linearly polarized laser to fast scan over the cavity eigenmodes. Our method excludes frequency

locking for a resonance driving, thus significantly reducing experimental complexity, and being particularly suitable for practical applications. In our setup, the temporal resolution is the applicable minimal measurement time, corresponding to the period scanning over a free spectral range (FSR). The scanning speed of the laser frequency is limited by the cavity response time, i.e. the inversion of linewidth. The spectral resolution is defined as the frequency interval between two neighboring data points. It is constrained by the uncertainty in numerically retrieving the position of the transmission peaks in fitting.

Next, we present a detailed explanation for our method of how to retrieve the ORD and CD by comparing the transmissions of the LCP and RCP eigenmodes. For the bowtie cavity with an effective round-trip length L , FSR is given by $\nu_{\text{FSR}} = c/L$, where c is the velocity of light. We use ν_L and ν_R for denoting the resonance frequencies of the LCP and RCP cavity eigenmodes, respectively. The input and output ports (mirrors) cause loss to the cavity, yielding the decay rates κ_1 and κ_2 , respectively. κ_i denotes the intrinsic loss rate of the cavity in the absence of the CM. The CM induces external decay rates κ_+ (κ_-) to the LCP (RCP) mode. The overall linewidths of the LCP and RCP modes are then given by $\kappa_L = (\kappa_1 + \kappa_2 + \kappa_i + \kappa_+)$ and $\kappa_R = (\kappa_1 + \kappa_2 + \kappa_i + \kappa_-)$, respectively. We consider a CM with length ℓ and concentration \mathcal{M} . For the solid phase sample, $\mathcal{M} = 1$ [46]. Using the standard cavity spectroscopy, we can obtain the transmission [47]:

$$T_x(\nu) = \frac{\kappa_1 \kappa_2}{(\nu - \nu_x)^2 + \kappa_x^2/4}, \quad (1)$$

with $x = L$ and $x = R$ for the LCP and RCP modes, respectively. The ORD can be evaluated as:

$$\Delta\varphi = \pi \frac{\nu_R - \nu_L}{\nu_{\text{FSR}}}. \quad (2)$$

The corresponding specific rotation of the CM is thus

$$\alpha = \Delta\varphi/\ell\mathcal{M}. \quad (3)$$

Using the relation $e^{-\xi_L \ell \mathcal{M}} = e^{-\kappa_+/\nu_{\text{FSR}}}$ and $e^{-\xi_R \ell \mathcal{M}} = e^{-\kappa_-/\nu_{\text{FSR}}}$ with ξ_L and ξ_R being the absorption coefficient of the LCP or RCP field in the CM, respectively (see Appendix), the CD can be characterized with the LCP and RCP absorption difference as $\Delta A = (\kappa_L - \kappa_R)/\nu_{\text{FSR}}$. Alternatively, one can use $\varepsilon = \Delta A/\ell\mathcal{M}$ for the CD. In practice, the CD can be calculated with the on-resonance transmission as

$$\Delta A = \frac{\kappa_L}{\nu_{\text{FSR}}} [1 - \sqrt{T_L(\nu_L)/T_R(\nu_R)}]. \quad (4)$$

Thus, the ORD and CD can be obtained by fitting the cavity transmission spectra of the LCP and RCP eigenmodes

with Lorentzian functions. By measuring the chiral eigenmode spectra $T_L(\nu)$ and $T_R(\nu)$, our method eliminates the requisite of a large magnetic field as a strong bias in the cavity ringdown polarimetry.

The possible eigenmode spectra are schematically presented in Fig. 2(c). The ORD, resulting from the circular birefringence of the CM, causes the LCP and RCP eigenmode spectra to shift oppositely. For a vanishing ORD, the eigenmodes are degenerate in resonance frequency, see subfigures (i, ii). For a right-handed material (v, vii), i.e. $\Delta\varphi > 0$, the RCP (LCP) resonance peaks move to right (left), corresponding to a higher (lower) resonance frequency. If the CM is left-handed (vi, viii), i.e. $\Delta\varphi < 0$, the spectral shifts reverse. The CD reflects the differential absorption of the LCP and RCP fields, and thus affects the transmission peak. For a CM without the CD, the transmission peak of the LCP and RCP are the same, see subfigures (iii, iv). According to our definition, a CM with positive CD, i.e. $\Delta A > 0$, leads to a RCP transmission higher than the LCP mode (v, vi). On the contrary, the LCP transmission is higher when the CD is negative, i.e. $\Delta A < 0$ (vii, viii).

2.2 Experimental setup and chiral spectroscopy

The experimental setup for measuring the ORD and CD is schematically shown in Fig. 3(a). A CM is placed between the input and output mirrors of the bowtie cavity. The bowtie cavity is fabricated with two high-reflectivity concave mirrors (diameter of 12.7 mm and curvature radius of 200 mm) and two planar mirrors. The concave and planar mirrors are coated with the dielectric distributed Bragg reflectors to have a high reflectivity of 97% and $\sim 100\%$, respectively. The planar side of the concave mirror is coated with an antireflective film. These mirrors are mounted on four three-dimensional positioners with resolution of 10 μm . The CM is placed at one of the cavity mode waists, locating at the center of the arm between M1 and M2. This position is optimal for measurement because the reduction of the cavity quality factor is minimized. In our experiment, we find that the cavity is stable and maintains the measurement performance as the CM moves within ± 20 mm with respect to this optimal position. A horizontally-polarized laser field with a power of 200 μW – 300 μW is incident into the bowtie cavity through the input mirror. It can be decomposed as the LCP and RCP components with the same amplitude, which excite the corresponding cavity modes. The transmitted LCP and RCP fields from the output mirror pass a quarter-wave plate and subsequently a polarization beam splitter and then is measured separately by two photodiodes. The data are collected by

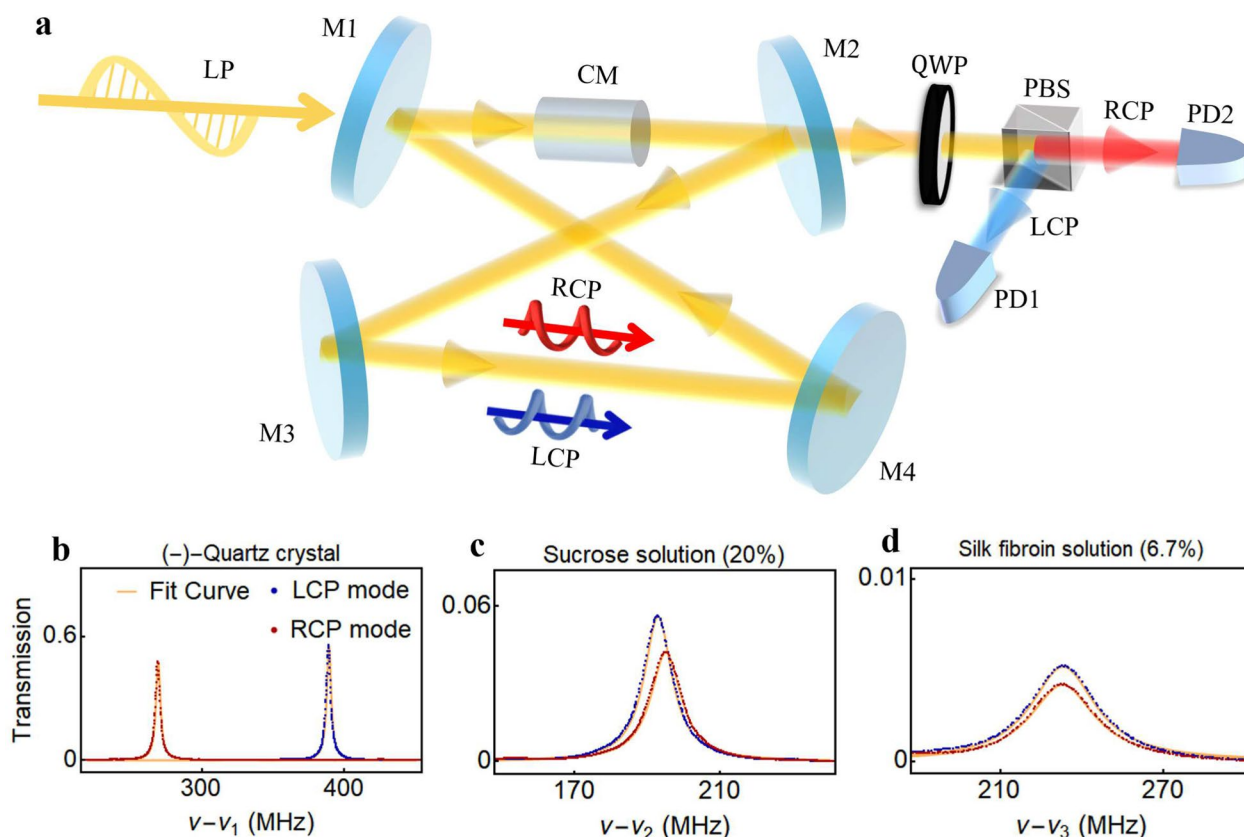


Fig. 3 Experimental setup and representative transmission spectra. **a**, schematic experimental setup. The setup consists of a combination of concave mirrors (M1, M2), planar mirrors (M3, M4), a chiral material (CM), a quarter-wave plate (QWP), a polarizing beam splitter (PBS), and photodiodes (PDs). **b, c, d** Typical transmission spectra for three different CMs: (-)-quartz crystal (**b**), sucrose solution (20%) (**c**), and silk fibroin solution (6.7%) (**d**). The LCP (blue dots) and RCP (red dots) transmissions are monitored by the PD1 and PD2, respectively. Experimental data is fitted (orange curves) according to Eq. 1. $\nu_1 = 379.48298$ THz, $\nu_2 = 379.46217$ THz, and $\nu_3 = 379.49126$ THz

an oscilloscope. Because of the CM, the LCP and RCP cavity eigenmodes have differential resonance frequency and linewidth. Thus, the LCP and RCP transmissions are different for the same laser frequency. We scan the laser frequency and record the transmission spectra. By fitting the transmission spectra, we retrieve the ORD and the CD of the CM. To exploit all energy of the incident light to generate signals, the waists of the eigenmodes and the laser beams need to be much smaller than the cross section of the CM. In the cavity ringdown polarimetry, a strong magnetic field is applied to induce a large difference in resonance frequency between the LCP and RCP eigenmodes. Thus, this magnetic field creates a large zero-signal bias for the beat frequency. In our method, the eigenmodes can be very close in resonance frequency when the ORD is very weak. To resolve the two orthogonal eigenmode spectra, our CECM spectroscopy completely separates them in outputs with a quarter-wave plate and a polarization beam splitter, forming a circular polarization beam splitter. Importantly, by doing so, the

two eigenmode spectra can be detected as they appear at completely different wavelengths. Thus, measurement of the chiral eigenmode spectra plays the role of an infinite magnetic field in the cavity ringdown polarimetry.

Examples of the eigenmode transmissions around $\lambda_0 = 790$ nm are shown in Fig. 3(b), (c), and (d) for three different CMs: (i) transparent solid-state (-)-quartz crystal, (ii) translucent sucrose solution (20%), and (iii) modest-opacity silk fibroin solution (6.7%), respectively. The finesses of the cavity are about 76.8, 29.7 and 11.2, respectively. The quartz crystal is 6 mm-long. The sucrose and silk fibroin solutions are contained in a 2 cm-long T-shaped glass tube. The quartz crystal (left-handed crystal) causes the LCP and RCP transmission spectra to split by many linewidth (~ 3.8 MHz). The transmission spectrum of the LCP component peaks at a higher frequency than the RCP component i.e. $\Delta\varphi < 0$, confirming that the inserted quartz crystal is left-handed. The higher LCP transmission peak indicates a negative CD, i.e. $\Delta A < 0$. The frequency splitting can also be distinguished in the

transmission of the composite field. For the sucrose and silk fibroin solution, the linewidths of the LCP and RCP modes increase to ~ 10.5 MHz and ~ 27.8 MHz, respectively. The spectra split by a mount much smaller than the transmission linewidth, thus is difficult to be precisely retrieved from the composite transmission spectrum. In stark contrast, by detecting the LCP and RCP transmission spectra separately and fitting them with Eq. 1, we can precisely determine the ORD and CD. Figures 3(c) and (d) show that the sucrose and silk fibroin solutions exhibit opposite ORD, corresponding to a right-handed material ($\Delta\varphi > 0$), and a left-handed material ($\Delta\varphi < 0$), but both negative CD, i.e. $\Delta A < 0$. Clearly, our method can simultaneously and precisely determine the ORD and CD from the eigenmode transmission spectra without the need of a magnetic field, even when they are too weak to be distinguished from the total transmitted field.

In our experiment, the input LCP and RCP components are very close in intensity. The transmitted eigenmode spectra are comparable in peak amplitude, even if they are well separate in frequency. Thus, our method can avoid weak measurement issues that one component is too weak to be detected efficiently.

2.3 Measurement of ORD and CD

Figure 4 show the ORD and CD spectra of four samples determined from the eigenmode transmissions. The ORD and CD are first measured over a large wavelength range between 765 nm and 800 nm with a wavelength interval of ~ 5 nm [Fig. 4(a), (c), (e) and (g)], and then around the wavelength $\lambda_0 = 790$ nm for a finer spectral resolution [Figs. 4(b), (d), (f) and (h)]. The cavity FSR is about 304 MHz. Each data point of the ORD and CD is calculated from a pair of the transmission spectra. Here, the

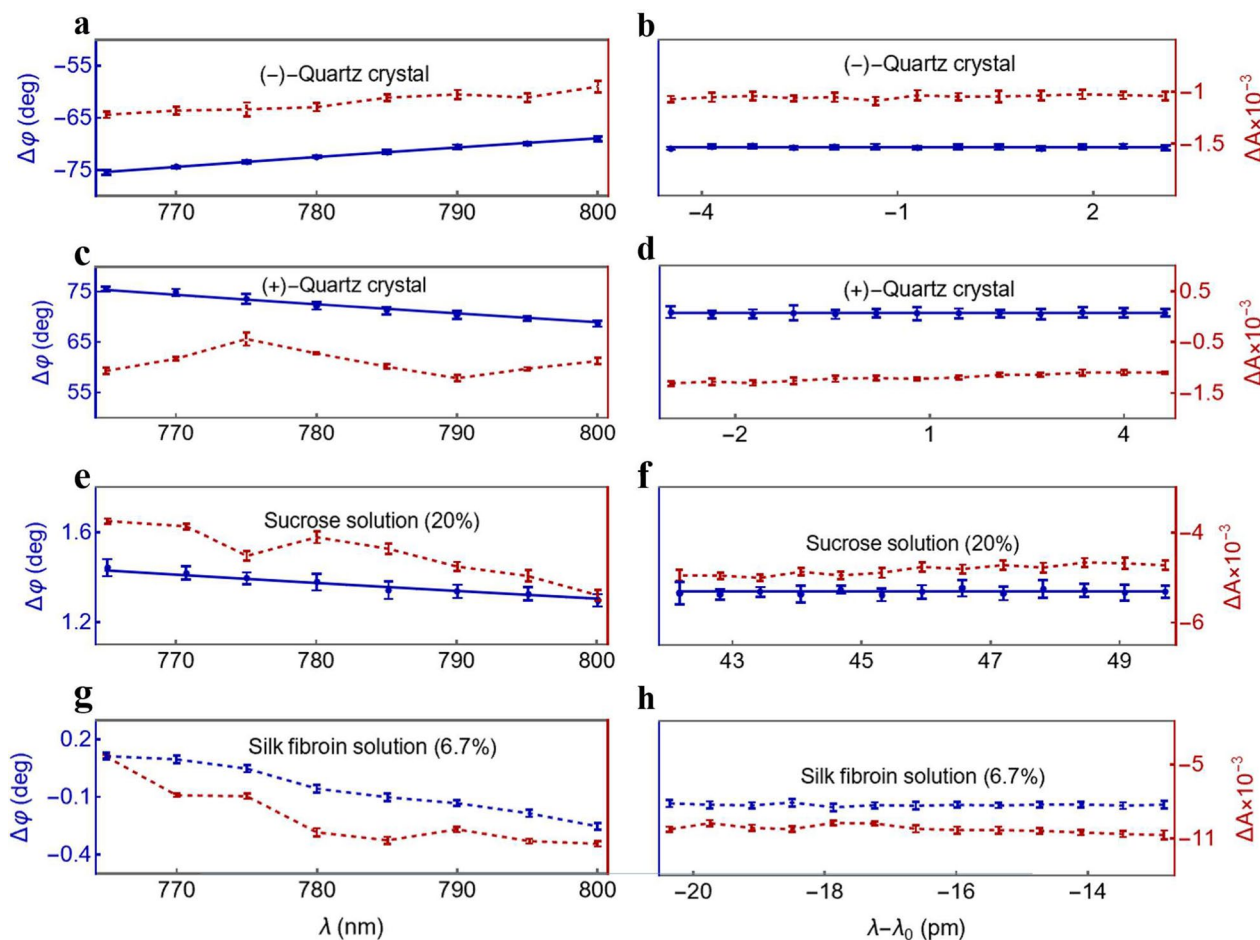


Fig. 4 ORD and CD spectra of (-)-quartz crystal, (+)-quartz crystal, sucrose solution (20%), and silk fibroin solution (6.7%) via the CECEM spectroscopy. **a, c, e, g**, The solid blue curves show the theoretical fittings using the formulas as in Refs. [48, 49]. The guide-to-eye dashed blue (dashed red) lines show the changes of ORD (CD) of the silk fibroin solution (four CMs) as the wavelength increases from 765 nm to 800 nm with a wavelength interval of ~ 5 nm. Each data point and its error bar are given by the mean and the standard deviation of 10 measurement data, respectively. **b, d, f, h**, For the fine scan near $\lambda_0 = 790$ nm with a spectral resolution of 0.63 pm, the ORD and CD spectra of the four CMs

spectral resolution is 0.63 pm. Although the scanning step size of the wavelength varies over a large range, the sensitivity remains stable. To measure the ORD and CD spectra shown in Figs. 4(b), (d), (f) and (h), we electrically scan the laser wavelength over 14.65 pm within 40 ms, corresponding to 7 GHz. Thus, scanning a FSR requires ~ 1.7 ms, which is also the time required for a single measurement.

For the (-)-quartz crystal, the ORD and CD decrease linearly, from $\Delta\varphi \approx -75.50$ deg to $\Delta\varphi \approx -67.95$ deg, and from $\Delta A \approx -1.2 \times 10^{-3}$ to $\Delta A \approx -0.8 \times 10^{-3}$, respectively, as the wavelength increases from 765 nm to 800 nm. In our case, we are able to detect a very weak CD. Specifically, at $\lambda - \lambda_0 = 1.8$ pm, the ORD and CD are $\Delta\varphi = -70.58 \pm 0.44$ deg and $\Delta A = (-1.03 \pm 0.04) \times 10^{-3}$ within a measurement time of $\tau = 16.6$ ms, respectively. The corresponding sensitivity is ~ 0.06 deg/ $\sqrt{\text{Hz}}$ for the ORD (a standard deviation of $\delta_{\Delta\varphi} = 0.44$ deg for $\tau = 16.6$ ms) and 5.2×10^{-6} / $\sqrt{\text{Hz}}$ for the CD (a standard deviation of $\delta_{\Delta A} = 4 \times 10^{-5}$ for $\tau = 16.6$ ms). Normally, according to the Cotton effect describing the optical activity near an absorption maximum [50], the signs of the ORD and CD reverse at the same time. Here, the (+)-quartz crystal displays opposite ORD and but also negative CD. This observation means that the signs of the ORD and CD are not necessarily correlated, because the crystal is transparent and thus far from the absorption peak. The experimental ORD data for the quartz over the infrared bands between 765 nm to 800 nm is excellently fitted by the formula $\Delta\varphi = \xi \ell \lambda^2 / (\lambda^2 - \lambda_0^2)^2$ as in Ref. [48] with $\xi = 7.35 \times 10^6$ deg nm²mm⁻¹ and $\lambda_0 = 92.6283$ nm, as shown by the solid blue curves in Figs. 4(a), (b), (c) and (d). Our method is firmly validated by this excellent agreement with the formula, which is widely used to model the CM. Note that the quartz crystals exhibit anisotropy. This measurement indicates that our method is applicable to an anisotropic CM. However, the measured optical activity may be dependent on the angle between the propagation direction of light and the optical axis of the anisotropic crystal. Considering the material anisotropy is typically tiny, the difference should be negligible if the angle is small.

Figure 4(e) presents the ORD and CD spectra of the 20% sucrose solution. The ORD decreases by 11.75% when the wavelength increases by 35 nm from $\lambda = 765$ nm. At $\lambda \sim 780$ nm, the ORD is $\Delta\varphi = 1.378 \pm 0.037$ deg for measuring 19.8 ms. This uncertainty corresponds to a resolvable concentration of 0.54% (0.0054 g/ml). Using the formula $\alpha = A / (\lambda^2 - \lambda_0^2)^2$ in Ref. [49] and Eq. 3 but setting $A = 2.03 \times 10^7$ deg nm²dm⁻¹g⁻¹ml and $\lambda_0 = 131$ nm, the experimental data is in good agreement with the theoretical values, see Figs. 4(e) and (f). The

sensitivity of $\Delta\varphi$ is $\sim 4.2 \times 10^{-3}$ deg/ $\sqrt{\text{Hz}}$. Moreover, the CD of the sucrose solution increases with the wavelength, but exhibits a valley of $\Delta A = (-4.53 \pm 0.10) \times 10^{-3}$ at $\lambda \sim 775$ nm. As shown in Fig. 4(g), the silk fibroin solution displays a very different optical activity from the sucrose solution. It changes from a weakly positive ORD, $\Delta\varphi \approx 0.11$ deg at 765 nm, to negative, $\Delta\varphi \approx -0.33$ deg at 800 nm. Meantime, its CD maintains negative. Taking $\lambda = 789.9853$ nm for a representative example, the ORD is $\Delta\varphi = -0.133 \pm 0.015$ deg and the CD is $\Delta A = (-10.39 \pm 0.22) \times 10^{-3}$, yielding a sensitivity of $\sim 2.1 \times 10^{-3}$ deg/ $\sqrt{\text{Hz}}$ and $\sim 3.1 \times 10^{-5}$ / $\sqrt{\text{Hz}}$, respectively. Figure 4(f) and (h) show the ORD and CD spectra within a range of 12 FSRs around 790 nm. The spectral resolution is up to ~ 0.63 pm. Note that the ORD and CD almost maintain constant because the spectral range only spans over ~ 7.65 pm. Nevertheless, these results demonstrate the capability of detecting a CM with very weak CD and high spectral resolution.

Figure 5(a) and (b) present the ORD and CD for different concentrations of sucrose solutions. Basically, the ORD and CD increases with the sucrose concentration, simply because the amount of the effective CM increases. After normalized by the concentration, the specific rotation of different samples is the same, about $\alpha = 34.45 \pm 0.94$ deg · dm⁻¹g⁻¹ml. Comparing Fig. 5(a) and (b), it can be seen that the ORD can determine the concentration more precisely. In contrast, the CD spectrum provides more characteristic information, showing an absorption valley at 775 nm. For precise chiroptical analysis of complex compounds, the CD spectroscopy has an advantage in distinguishing the different ingredients. The minimum resolvable concentration of solution is determined by the sensitivity and the measurement time. When the scan speed of laser frequency is fixed, the sensitivity relies on the uncertainty in extracting the resonance frequency by fitting the eigenmode spectra. Thus, a cavity with higher quality factor is preferable. However, the solution is absorptive and limits the available quality factor. This can be seen from the low transmission in Fig. 3(c). We can improve the resolvable concentration by increasing the measurement time.

By adjusting the resonant frequency of the cavity, we can measure the ORD and CD with a spectral resolution much smaller than the cavity FSR at a special wavelength of interest. In this case, the spectral resolution is improved to the adjustment interval of the resonance frequency. As a proof-of-principle demonstration, Fig. 5(c) displays the eigenmode transmission spectra for three differential cavity lengths. The eigenmode transmission pairs shift slightly in frequency. The ORD and CD are retrieved from these three pairs of transmission spectra. Their frequency difference indicate a spectral

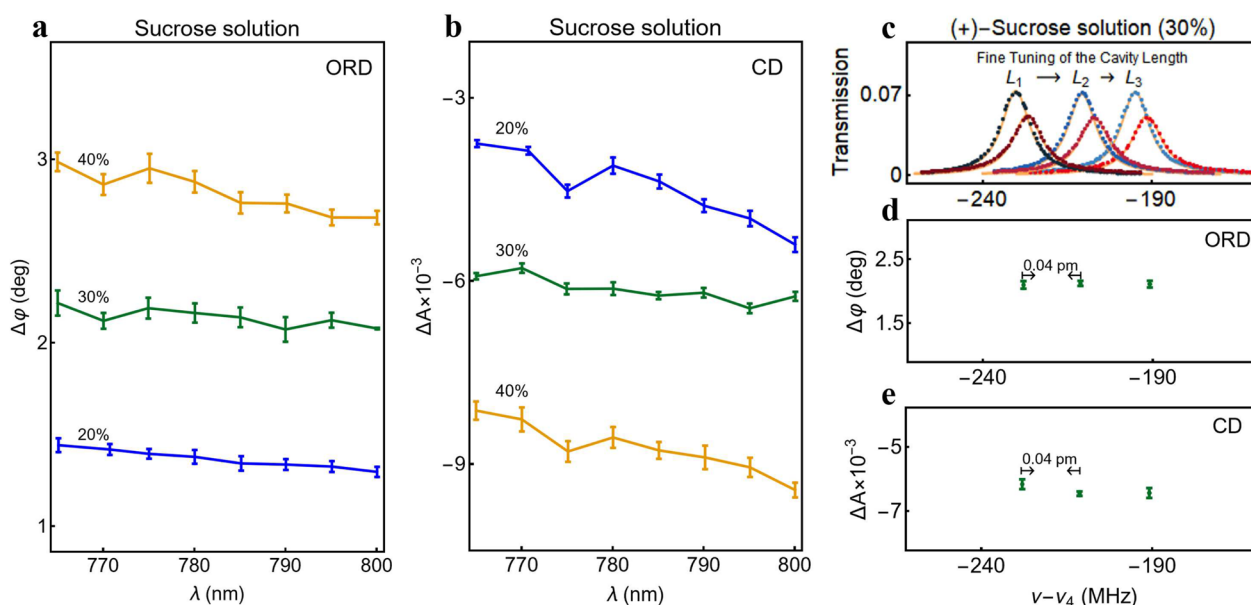


Fig. 5 Chiral analysis and improvement of the spectral resolution. **a, b**, The ORD and CD for different concentrations of sucrose solutions. **c, d, e**, The cavity transmission spectrum after fine tuning the cavity length around central frequencies $\nu_4 = 379.48281$ THz (**c**), and the corresponding ORD (**d**) and CD (**e**). The blue dots indicate the LCP mode, the red dots indicate the RCP mode, and the orange curve indicates the fitted by Eq. 1

resolution up to ~ 0.04 pm, see Fig. 5(d) and (e). This resolution is one order better than the FSR. Meanwhile, we increase the electrically scanning speed of the laser frequency up to 1.045 GHz/ms, so high sensitivity of $\sim 2.7 \times 10^{-3}$ deg/ $\sqrt{\text{Hz}}$ (a standard deviation of $\delta_{\Delta\varphi} = 0.05$ deg for $\tau = 2.9$ ms) and $\sim 8.1 \times 10^{-6}$ / $\sqrt{\text{Hz}}$ (a standard deviation of $\delta_{\Delta A} = 1.5 \times 10^{-4}$ for $\tau = 2.9$ ms) are obtained for the ORD and CD, respectively. These results further confirm the potential of our technology for fast measuring the optical activity with high spectral resolution.

3 Discussion and conclusion

Simultaneous measurement of absolute ORD and CD with high sensitivity, high temporal and spectral resolution contributes to the development of many applications, such as precise assembly and construction of chiral molecules, synthesis of complex chiral drugs, and characterization of chiral supramolecules and macromolecules [35, 51, 52]. First, the high sensitivity can be applied to the drug analysis, the authentication and adulteration of low concentration CMs [23]. Also, the precision in our measurement of the specific rotation is comparable to previous studies [32, 45], but our scheme does not require a highly stabilized cavity and precise modulation of the magnetic field. Secondly, the millisecond-level temporal resolution could potentially be used to monitor protein folding and chemical mechanisms in living cells. Moreover, our setup enables

real-time monitoring of dynamic chemical reactions without any mechanical adjustments. Thirdly, the sub-picometer spectral resolution measurements provide a tool to study the fine characteristic spectrum of ORD and CD, which may be used to obtain the finer fingerprint information of biomolecules [53].

This magnetic-free CECM spectroscopy may also be conducted by inserting two quarter-wave plates in the standard FP cavity, each between the CM and the input-output mirror. The schematic setup and specific operation are detailedly explained in the supplementary information. If the two wave plates can be precisely aligned with parallel optical axes, one can, in principle, measure the eigenmode spectra and determine the ORD and CD of the CM. However, operation and alignment of the wave plates can be complicated [35, 54].

We have reported the simultaneous measurement of the ORD and CD of CMs obtained via the magnetic-free CECM spectroscopy. This method reaches a remarkably high spectral resolution up to 0.04 pm, corresponding to 20 MHz. This work also demonstrated ultrahigh sensitivities for both ORD and CD within a few millisecond measurement time. It paves the way for fast chiroptical analysis of chemistry, biology and pharmacology with high spectral resolution and sensitivity.

Appendix A: The derivation of optical rotary dispersion

The linearly polarized light consists of LCP and RCP components with equal intensity. After passing through the CM, the two circularly polarized components will have different phase shifts $\varphi_L = 2\pi n_L \ell \cdot \nu/c$ and $\varphi_R = 2\pi n_R \ell \cdot \nu/c$, respectively, where n_L and n_R are the refractive indexes of the LCP and RCP components, ℓ is the length of the CM, and ν is the frequency of the input linearly polarized light. The ORD, i.e. the ability of a CM to rotate the plane of vibration of the polarized light, can be described by introducing a general form for the difference of phase shifts of RCP and LCP components:

$$\Delta\varphi = \frac{1}{2}(\varphi_L - \varphi_R) = \frac{\pi\nu}{c}(n_L - n_R)\ell, \quad (\text{S1})$$

where $\Delta\varphi$ is the rotation angle of the plane-polarized light. In a bowtie cavity with a CM, the difference of resonant frequencies of LCP and RCP components can be expressed as

$$(n_L - n_R)\ell = \frac{\nu}{\nu_{\text{FSR}}}\left(\frac{c}{\nu_L} - \frac{c}{\nu_R}\right), \quad (\text{S2})$$

where ν_L (ν_R) is the resonant frequency of LCP (RCP) component, $\Delta\nu_{\text{FSR}}$ is the cavity's free spectral range. If $\nu_L - \nu_R \ll \nu_L$ or ν_R , it can be approximated that $\nu_L \nu_R \approx \nu^2$. Then, according to Eqs. S1 and S2, the ORD ($\Delta\varphi$) is given by

$$\Delta\varphi = \pi \frac{\nu_R - \nu_L}{\nu_{\text{FSR}}}. \quad (\text{S3})$$

Appendix B: The derivation of circular dichroism

For the bowtie cavity, the cavity transmitted of the LCP and RCP modes can be written as Eq. 1. $\kappa_L - \kappa_R = \kappa_+ - \kappa_-$ corresponds to the difference in absorption of the CM for LCP and RCP components. The CD can be expressed by the difference in absorbance of the LCP component and the RCP component as

$$\Delta\xi = \xi_L - \xi_R, \quad (\text{S4})$$

where ξ_L (ξ_R) is the absorption coefficient of the LCP (RCP) component. Furthermore, noting that $I = I_0 e^{-\xi_L \ell \mathcal{M}} = I_0 e^{-\kappa_+/\nu_{\text{FSR}}}$ and $I = I_0 e^{-\xi_R \ell \mathcal{M}} = I_0 e^{-\kappa_-/\nu_{\text{FSR}}}$, the absorption coefficient can hence be written as

$$\xi_{L/R} = \frac{\kappa_{+/-}}{\nu_{\text{FSR}} \ell \mathcal{M}}. \quad (\text{S5})$$

According to Eqs. S4 and S5, the CD (ΔA) is then given by

$$\Delta A = \Delta\xi \times \ell \mathcal{M} = \frac{\kappa_+ - \kappa_-}{\nu_{\text{FSR}}} = \frac{\kappa_L - \kappa_R}{\nu_{\text{FSR}}}. \quad (\text{S6})$$

Further, according to Eq. 1, there are $\kappa_R = \kappa_L \sqrt{T_L(\nu_L)/T_R(\nu_R)}$. Substituting into Eqs. S6, the following can be obtained

$$\Delta A = \frac{\kappa_L}{\nu_{\text{FSR}}} [1 - \sqrt{T_L(\nu_L)/T_R(\nu_R)}]. \quad (\text{S7})$$

Abbreviations

ORD:	Optical rotary dispersion
CD:	Circular dichroism
CM:	Chiral material
RCP:	Right circularly polarized
LCP:	Left circularly polarized
CECEM:	Cavity-enhanced chiral eigenmode
FP:	Fabry-Pérot
FSR:	Free spectral range

Supplementary Information

The online version contains supplementary material available at <https://doi.org/10.1186/s43593-024-00068-4>.

Supplementary material file 1.

Acknowledgements

This work was supported by the National Key R&D Program of China (Grants No. 2022YFA1405000, No. 2019YFA0308700), the National Natural Science Foundation of China (Grants No. 92365107, No. 12305020, and No. 11890704), the Program for Innovative Talents and Teams in Jiangsu (Grant No. JSSCTD202138), and the Innovation Program for Quantum Science and Technology (Grant No. 2021ZD0301400). China Postdoctoral Science Foundation (Grant No. 2023M731613), and Jiangsu Funding Program for Excellent Postdoctoral Talent (Grant No. 2023ZB708). C.-W.Q. is supported by the Competitive Research Program Award (NRF-CRP22-2019-0006 & NRF-CRP26-2021-0004) from the NRF, Prime Minister's Office, Singapore, and by a grant (A-0005947-16-00) from A*STAR MTC IRG (M22K2c0088 with A-8001322-00-00).

Author contributions

K.X. and Y.-P.R. conceived the original idea. K.X., H.Z. and C.-W.Q. designed research. W.Z. conducted the experiment and contributed to the theoretical model. K.X., Y.-Q.L. and C.-W.Q. contributed to refining the original idea and co-supervised the project. H.W., and H.Z. partly conducted the experiment and especially the bowtie cavity. L.T. contributed to the original idea. K.X., L.T., J.-S.T. and C.-W.Q. contributed the theoretical model and analysis. Z.X. and K.J. provided the concave mirrors for this experiment. Y.W. and Y.-E.J. provided the silk fibroin solution. All authors contributed to discussions of the results and writing of the manuscript.

Data availability

All data needed to evaluate the conclusions are present in the paper and/or the Supplementary Materials. Additional data related to this paper are available from the corresponding author on reasonable request.

Declaration

Competing interests

Cheng-Wei Qiu serves as an Editor for the Journal, no other author has reported any competing interests.

Received: 26 January 2024 Revised: 6 May 2024 Accepted: 16 May 2024

Published online: 12 July 2024

References

- R.M. Kim, J.-H. Huh, S. Yoo, T.G. Kim, C. Kim, H. Kim, J.H. Han, N.H. Cho, Y.-C. Lim, S.W. Im, E. Im, J.R. Jeong, M.H. Lee, T.-Y. Yoon, H.-Y. Lee, Q.-H. Park, S. Lee, K.T. Nam, Enantioselective sensing by collective circular dichroism. *Nature* 612, 470–476 (2022). <https://doi.org/10.1038/s41586-022-05353-1>
- D. Lee, S. So, G. Hu, M. Kim, T. Badloe, H. Cho, J. Kim, H. Kim, C.-W. Qiu, J. Rho, Hyperbolic metamaterials: fusing artificial structures to natural 2D materials. *eLight* 2, 1–23 (2022). <https://doi.org/10.1186/s43593-021-00008-6>
- A.Y. Zhu, W.T. Chen, A. Zaidi, Y.-W. Huang, M. Khorasaninejad, V. Sanjeev, C.-W. Qiu, F. Capasso, Giant intrinsic chiro-optical activity in planar dielectric nanostructures. *Light Sci Appl* 7, 17158–17158 (2018). <https://doi.org/10.1038/lsa.2017.158>
- S. Zhou, J. Bian, P. Chen, M. Xie, J. Chao, W. Hu, Y. Lu, W. Zhang, Polarization-dispersive imaging spectrometer for scattering circular dichroism spectroscopy of single chiral nanostructures. *Light Sci Appl* 11, 1–7 (2022). <https://doi.org/10.1038/s41377-022-00755-2>
- K. Xia, G. Lu, G. Lin, Y. Cheng, Y. Niu, S. Gong, J. Twamley, Reversible non-magnetic single-photon isolation using unbalanced quantum coupling. *Phys Rev A* 90, 043802 (2014). <https://doi.org/10.1103/PhysRevA.90.043802>
- S. Zhang, Y. Hu, G. Lin, Y. Niu, K. Xia, J. Gong, S. Gong, Thermal-motion-induced non-reciprocal quantum optical system. *Nat Photon* 12, 744–748 (2018). <https://doi.org/10.1038/s41566-018-0269-2>
- P. Lodahl, S. Mahmoodian, S. Stobbe, A. Rauschenbeutel, P. Schneeweiss, J. Volz, H. Pichler, P. Zoller, Chiral quantum optics. *Nature* 541, 473–480 (2017). <https://doi.org/10.1038/nature21037>
- J.-S. Tang, W. Nie, L. Tang, M. Chen, X. Su, Y. Lu, F. Nori, K. Xia, Nonreciprocal single-photon band structure. *Phys Rev Lett* 128, 203602 (2022). <https://doi.org/10.1103/PhysRevLett.128.203602>
- J.T. Pelton, L.R. McLean, Spectroscopic methods for analysis of protein secondary structure. *Anal Biochem* 277, 167–176 (2000). <https://doi.org/10.1006/abio.1999.4320>
- S. Beychok, Circular dichroism of biological macromolecules: circular dichroism spectra of proteins and nucleic acids provide insights into solution conformations. *Science* 154, 1288–1299 (1966). <https://doi.org/10.1126/science.154.3754.1288>
- H.J. Eckvahl, N.A. Tcyrulnikov, A. Chiesa, J.M. Bradley, R.M. Young, S. Carretta, M.D. Krzyaniak, M.R. Wasielewski, Direct observation of chirality-induced spin selectivity in electron donor-acceptor molecules. *Science* 382, 197–201 (2023). <https://doi.org/10.1126/science.adj5328>
- R. Naaman, Y. Paltiel, D.H. Waldeck, Chiral molecules and the electron spin. *Nat Rev Chem* 3, 250–260 (2019). <https://doi.org/10.1038/s41570-019-0087-1>
- Y. Chen, H. Deng, X. Sha, W. Chen, R. Wang, Y.-H. Chen, D. Wu, J. Chu, Y.S. Kivshar, S. Xiao et al., Observation of intrinsic chiral bound states in the continuum. *Nature* 613, 474–478 (2023). <https://doi.org/10.1038/s41586-022-05467-6>
- L.D. Barron, *Molecular light scattering and optical activity* (Cambridge University Press, Cambridge, 2009)
- J.-L. Bégin, A. Jain, A. Parks, F. Hufnagel, P. Corkum, E. Karimi, T. Brabec, R. Bhardwaj, Nonlinear helical dichroism in chiral and achiral molecules. *Nat Photon* 17, 1–7 (2022). <https://doi.org/10.1038/s41566-022-01100-0>
- B.A. McGuire, P.B. Carroll, R.A. Loomis, I.A. Finneran, P.R. Jewell, A.J. Remijan, G.A. Blake, Discovery of the interstellar chiral molecule propylene oxide (ch₃chch₂o). *Science* 352, 1449–1452 (2016). <https://doi.org/10.1126/science.aae0328>
- S.M. Kelly, T.J. Jess, N.C. Price, How to study proteins by circular dichroism. *Biochim. Biophys. Acta Proteins Proteom* 1751, 119–139 (2005). <https://doi.org/10.1016/j.bbapap.2005.06.005>
- Y.H. Lee, Y. Won, J. Mun, S. Lee, Y. Kim, B. Yeom, L. Dou, J. Rho, J.H. Oh, Hierarchically manufactured chiral plasmonic nanostructures with gigantic chirality for polarized emission and information encryption. *Nat Commun* 14, 7298 (2023). <https://doi.org/10.1038/s41467-023-43112-6>
- H.-E. Lee, R.M. Kim, H.-Y. Ahn, Y.Y. Lee, G.H. Byun, S.W. Im, J. Mun, J. Rho, K.T. Nam, Cysteine-encoded chirality evolution in plasmonic rhombic dodecahedral gold nanoparticles. *Nat Commun* 11, 263 (2020). <https://doi.org/10.1038/s41467-019-14117-x>
- M.E. Franks, G.R. Macpherson, W.D. Figg, Thalidomide. *Lancet* 363, 1802–1811 (2004). [https://doi.org/10.1016/S0140-6736\(04\)16308-3](https://doi.org/10.1016/S0140-6736(04)16308-3)
- H. Rhee, J.S. Choi, D.J. Starling, J.C. Howell, M. Cho, Amplifications in chiroptical spectroscopy, optical enantioselectivity, and weak value measurement. *Chem Sci* 4, 4107–4114 (2013). <https://doi.org/10.1039/C3SC51255J>
- L. Tang, J. Tang, M. Chen, F. Nori, M. Xiao, K. Xia, Quantum squeezing induced optical nonreciprocity. *Phys Rev Lett* 128, 083604 (2022). <https://doi.org/10.1103/PhysRevLett.128.083604>
- N.J. Greenfield, Using circular dichroism spectra to estimate protein secondary structure. *Nat Protoc* 1, 2876–2890 (2006). <https://doi.org/10.1038/nprot.2006.202>
- Y. Chen, C. Zhao, Y. Zhang, C. Qiu, Integrated molar chiral sensing based on high-Q metasurface. *Nano Lett* 20, 8696–8703 (2020). <https://doi.org/10.1021/acs.nanolett.0c03506>
- T. Liu, C. Guo, W. Li, S. Fan, Thermal photonics with broken symmetries. *eLight* 2, 25 (2022). <https://doi.org/10.1186/s43593-022-00025-z>
- H. Lee, A. Kecebas, F. Wang, L. Chang, S.K. Özdemir, T. Gu, Chiral exceptional point and coherent suppression of backscattering in silicon microring with low loss mie scatterer. *eLight* 3, 20 (2023). <https://doi.org/10.1186/s43593-023-00043-5>
- H. Rhee, Y.-G. June, J.-S. Lee, K.-K. Lee, J.-H. Ha, Z.H. Kim, S.-J. Jeon, M. Cho, Femtosecond characterization of vibrational optical activity of chiral molecules. *Nature* 458, 310–313 (2009). <https://doi.org/10.1038/nature07846>
- D. Peng, C. Gu, Z. Zuo, Y. Di, X. Zou, L. Tang, L. Deng, D. Luo, Y. Liu, W. Li, Dual-comb optical activity spectroscopy for the analysis of vibrational optical activity induced by external magnetic field. *Nat Commun* 14, 883 (2023). <https://doi.org/10.1038/s41467-023-36509-w>
- D. Patterson, M. Schnell, J.M. Doyle, Enantiomer-specific detection of chiral molecules via microwave spectroscopy. *Nature* 497, 475–477 (2013). <https://doi.org/10.1038/nature12150>
- L. Ohnoutek, N.H. Cho, A.W. Allen Murphy, H. Kim, D.M. Răsădean, G.D. Pantoş, K.T. Nam, V.K. Valev, Single nanoparticle chiroptics in a liquid: Optical activity in hyper-rayleigh scattering from au helicoids. *Nano Lett* 20, 5792–5798 (2020). <https://doi.org/10.1021/acs.nanolett.0c01659>
- Y. Chen, W. Chen, X. Kong, D. Wu, J. Chu, C.-W. Qiu, Can weak chirality induce strong coupling between resonant states? *Phys Rev Lett* 128, 146102 (2022). <https://doi.org/10.1103/PhysRevLett.128.146102>
- D.-B.-A. Tran, K.M. Manfred, R. Peverall, G.A.D. Ritchie, Continuous-wave cavity-enhanced polarimetry for optical rotation measurement of chiral molecules. *Anal Chem* 93, 5403–5411 (2021). <https://doi.org/10.1021/acs.analchem.0c04651>
- L. Bougas, J. Byron, D. Budker, J. Williams, Absolute optical chiral analysis using cavity-enhanced polarimetry. *Sci Adv* 8, 3749 (2022). <https://doi.org/10.1126/sciadv.abm3749>
- D. Sofikitis, L. Bougas, G.E. Katsoprinakis, A.K. Spiliotis, B. Loppinet, T.P. Rakitzis, Evanescent-wave and ambient chiral sensing by signal-reversing cavity ringdown polarimetry. *Nature* 514, 76–79 (2014). <https://doi.org/10.1038/nature13680>
- T. Müller, K.B. Wiberg, P.H. Vaccaro, Cavity ring-down polarimetry (CRDP): a new scheme for probing circular birefringence and circular dichroism in the gas phase. *J Phys Chem A* 104, 5959–5968 (2000). <https://doi.org/10.1021/jp000705n>
- A.K. Singh, Z.-H. Lin, M. Jiang, T.G. Mayerhöfer, J.-S. Huang, Dielectric metasurface-assisted cavity ring-down spectroscopy for thin-film circular dichroism analysis. *Nanoscale* 15, 14093–14099 (2023). <https://doi.org/10.1007/BF03052717>
- F. Preda, A. Perri, J. Réhault, B. Dutta, J. Helbing, G. Cerullo, D. Polli, Time-domain measurement of optical activity by an ultrastable common-path

- interferometer. *Opt Lett* 43, 1882–1885 (2018). <https://doi.org/10.1364/OL.43.001882>
38. H. Rhee, Y.-G. June, Z.H. Kim, S.-J. Jeon, M. Cho, Phase sensitive detection of vibrational optical activity free-induction-decay: vibrational cd and ord. *J Opt Soc Am B* 26, 1008–1017 (2009). <https://doi.org/10.1364/JOSAB.26.001008>
 39. S. Ghosh, G. Herink, A. Perri, F. Preda, C. Manzoni, D. Polli, G. Cerullo, Broad-band optical activity spectroscopy with interferometric fourier-transform balanced detection. *ACS photon* 8, 2234–2242 (2021). <https://doi.org/10.1021/acsp Photonics.0c01866>
 40. R. Peverall, S. Rosson, K.M. Manfred, G.A. Ritchie, High performance continuous-wave laser cavity enhanced polarimetry using RF-induced linewidth broadening. *Opt Express* 29, 30114–30122 (2021). <https://doi.org/10.1364/OE.435006>
 41. A. Lakhani, P. Malon, T.A. Keiderling, Comparison of vibrational circular dichroism instruments: development of a new dispersive vcd. *Appl Spectrosc* 63, 775–785 (2009). <https://doi.org/10.1366/000370209788701189>
 42. A. Kastner, G. Koumariou, P. Glodic, P.C. Samartzis, N. Ladda, S.T. Ranecky, T. Ring, S. Vasudevan, C. Witte, H. Braun, H.-G. Lee, A. Senftleben, R. Berger, G.B. Park, T. Schäfer, T. Baumert, High-resolution resonance-enhanced multiphoton photoelectron circular dichroism. *Phys Chem Chem Phys* 22, 7404–7411 (2020). <https://doi.org/10.1039/D0CP00470G>
 43. A. Sargsyan, A. Amiryan, A. Tonoyan, E. Klinger, D. Sarkisyan, Circular dichroism in atomic vapors: magnetically induced transitions responsible for two distinct behaviors. *Phys Rev A* 390, 127114 (2021). <https://doi.org/10.1016/j.physleta.2020.127114>
 44. P.J. Visser, J. Levallois, M.K. Tran, J.-M. Poumirol, I.O. Nedoliuk, J. Teyssier, C. Uher, D. Van Der Marel, A.B. Kuzmenko, Suppressed magnetic circular dichroism and valley-selective magnetoabsorption due to the effective mass anisotropy in bismuth. *Phys Rev Lett* 117, 017402 (2016). <https://doi.org/10.1103/PhysRevLett.117.017402>
 45. L. Bougas, D. Sofikitis, G.E. Katsoprinakis, A.K. Spiliotis, P. Tzallas, B. Loppinet, T.P. Rakitzis, Chiral cavity ring down polarimetry: chirality and magnetometry measurements using signal reversals. *J Chem Phys* 143, 104202 (2015). <https://doi.org/10.1063/1.4930109>
 46. E.U. Condon, Theories of optical rotatory power. *Rev Mod Phys* 9, 432–457 (1937). <https://doi.org/10.1103/RevModPhys.9.432>
 47. D. Walls, G.J. Milburn, *Quantum Optics* (Springer, Berlin, 2008)
 48. S. Chandrasekhar, The optical rotatory dispersion of quartz. *Proc Ind Acad Sci* (1957). <https://doi.org/10.1007/BF03052717>
 49. R.N. Compton, S.M. Mahurin, R.N. Zare, Demonstration of optical rotatory dispersion of sucrose. *J Chem Educ* 76, 1234 (1999). <https://doi.org/10.1021/ed076p1234>
 50. V.K. Ahluwalia, *Optical rotatory dispersion and circular dichroism* (Springer, Cham, 2022)
 51. Y. Zhao, A.N. Askarpour, L. Sun, J. Shi, X. Li, A. Alù, Chirality detection of enantiomers using twisted optical metamaterials. *Nat Commun* 8, 1–8 (2017). <https://doi.org/10.1038/ncomms14180>
 52. N.A. Oktaviani, A. Matsugami, A.D. Malay, F. Hayashi, D.L. Kaplan, K. Numata, Conformation and dynamics of soluble repetitive domain elucidates the initial β -sheet formation of spider silk. *Nat Commun* 9, 2121 (2018). <https://doi.org/10.1038/s41467-018-04570-5>
 53. D. Etezadi, J.B. Warner IV, F.S. Ruggeri, G. Dietler, H.A. Lashuel, H. Altug, Nanoplasmonic mid-infrared biosensor for in vitro protein secondary structure detection. *Light Sci Appl* 6, 17029–17029 (2017). <https://doi.org/10.1038/lsa.2017.29>
 54. T. Müller, K.B. Wiberg, P.H. Vaccaro, J.R. Cheeseman, M.J. Frisch, Cavity ring-down polarimetry (CRDP): theoretical and experimental characterization. *J Opt Soc Am B* 19, 125–141 (2002). <https://doi.org/10.1364/JOSAB.19.000125>